Supplementary Material

Ultrathin NiCo-LDH regulated by CuNiCo trimetallic spinel sulfides as highly active and stable electrocatalysts for overall water splitting

Xinyuan Yu, Jiaying Shen, Qianqiao Chen, and Qin Zhong*

College of Chemistry and Chemical Engineering, Nanjing University of Science and Technology, Nanjing, 210094, People's Republic of China

*Email: cqq@njust.edu.cn

1. Experimental section

1.1. Synthesis of heterostructures with different electrodeposition times

Two other heterostructures (NiCo-LDH-600s/CuNiCo-S/NF and NiCo-LDH-1200s/CuNiCo-S/NF) with different deposition times were prepared, with electrodeposition times of 600s and 1200s, and the rest of the preparation process was consistent with NiCo-LDH/CuNiCo-S/NF.

1.2. Synthesis of the $NiCo_2S_4$/NF

$NiCo_2S_4$/NF was prepared using the same method and parameters as CuNiCo-S/NF, but without the $Cu(NO_3)_2 \cdot 3H_2O$.

1.3. Synthesis of the NiCo-LDH/NF

The synthesis process of NiCo-LDH/NF was similar to NiCo-LDH/CuNiCo-S/NF, simply replacing the working electrode CuNiCo-S/NF with NF.

1.4. Synthesis of the NiCo-LDH/$NiCo_2S_4$/NF

NiCo-LDH/$NiCo_2S_4$/NF was prepared using the same method and parameters of NiCo-LDH/CuNiCo-S/NF, but without the $Cu(NO_3)_2 \cdot 3H_2O$.

1.5. Synthesis of the RuO_2/NF

Firstly, 4mg RuO_2 powder was dissolved in 10mL ethanol and sonicated for 30 minutes, then 5mL solution was evenly dropped onto 2×1cm NF with a pipette, and finally, RuO_2/NF was obtained after air-drying at room temperature.

1.6. Synthesis of the Pt/C/NF

Firstly, 4mg 20wt% Pt/C powder was dissolved in 10mL ethanol and sonicated for 30

minutes, then 5mL solution was evenly dropped onto 2×1cm NF with a pipette, and finally, Pt/C/NF was obtained after air-drying at room temperature.

1.7. Characterization

Scanning electron microscope (SEM; Hitachi S4800) and transmission electron microscope (TEM; JEM2100F) were used to study the morphology and structure of the samples. The crystallographic information of samples was characterized by X-ray diffraction (XRD; Bruker AXS GmbH, D8ADVANCE, Cu Ka radiation). The chemical state and surface compositions were analyzed by X-ray photoelectron spectroscopy (XPS; Thermo, ESCALAB 250Xi) using a monochromatic Al Ka as the X-ray source. Inductively coupled plasma mass spectrometry (ICP-MS) was used to obtain the elemental composition of the samples. The contact angle was measured by an instrument JC2000D.

1.8. Electrochemical measurement

All electrochemical tests were measured by a three-electrode system, which was connected to an Ivium-N-Stat electrochemical workstation. The synthesized samples were used as the working electrode, a graphite rod was applied as the auxiliary electrode and a saturated calomel electrode (SCE) was utilized as the reference electrode.1.0 M KOH electrolyte which was injected N_2 for 30 min was used as the electrolyte for all electrochemical measurements. For the OER tests, all linear-sweep voltammograms (LSV) were measured from 0 to 0.8 V (vs. SCE) at a scan rate of 2 $mV \cdot s^{-1}$. The HER activities of samples were assessed by the linear sweep voltammetry (LSV) from -1 to -1.6 V (vs. SCE) with a scan rate of 2 $mV \cdot s^{-1}$. The stability of the samples was tested by two modes of

chronopotentiometry measurements, one was carried out at an invariable current for 48 h, and the other was applied current from 50 to 10 $mA \cdot cm^{-2}$ with an increment of 10 $mA \cdot cm^{-2}$ per 8 h. The electrochemical impedance spectroscopy (EIS) was conducted at the frequency range of 0.1 MHz to 0.1 Hz with an amplitude of 5 mV. All potential in these tests was transformed by the equation ($E_{RHE}=E_{SCE}+0.241+0.059pH$). All polarization curves were performed with 95% *i*R-correction. $E_{corrected}=E_{measured}-j\times R\times S$, $E_{corrected}$ is the corrected potential, $E_{measured}$ is the measured potential, j is the current density, R is the ohmic drop measured by the electrochemical impedance spectroscopy, S is the geometric area of the catalytic electrode. The electrochemical surface areas (ECSAs) of the electrodes were expressed by the double-layer capacitance values (C_{dl}). The C_{dl} was tested by the cyclic voltammograms (CVs) with different scan rates (20, 40, 60, 80, and 100 $mV \cdot s^{-1}$) in the potential range from -1.05 to -0.85 V (vs. SCE). The Faraday efficiency (FE) was acquired according to the following formula[1]:

$$FE = \frac{V_{exp.}}{V_{the.}} \times 100\%$$

where $V_{exp.}$ is the experimental volume of O_2 or H_2, $V_{the.}$ is the theoretical volume of O_2 or H_2.

2. Supplementary Figures and Tables

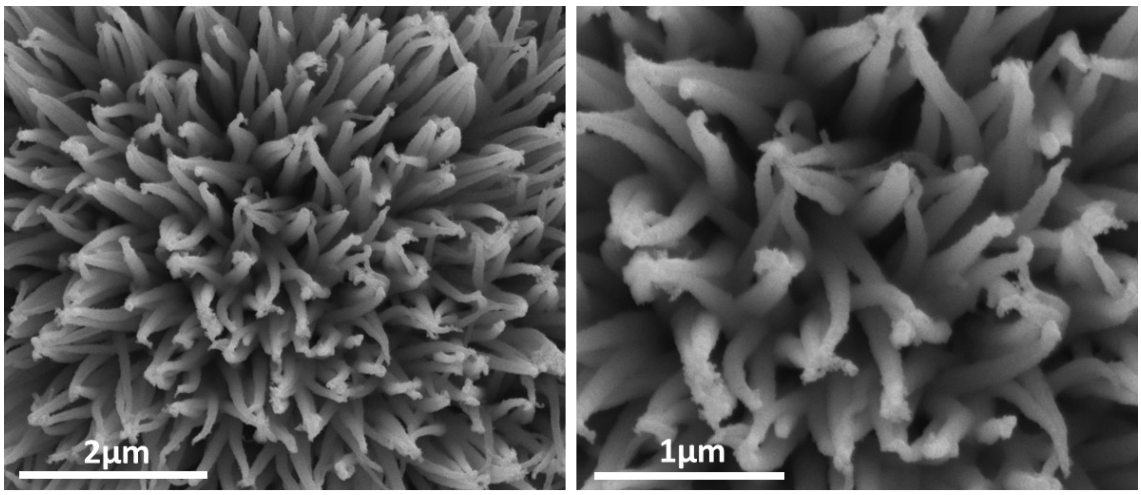

Figure S1. The SEM images of CuNiCo-S/NF.

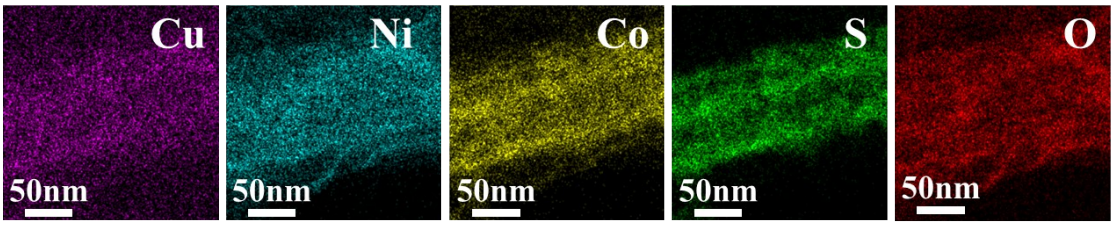

Figure S2. Higher resolution element mapping of NiCo-LDH/CuNiCo-LDH.

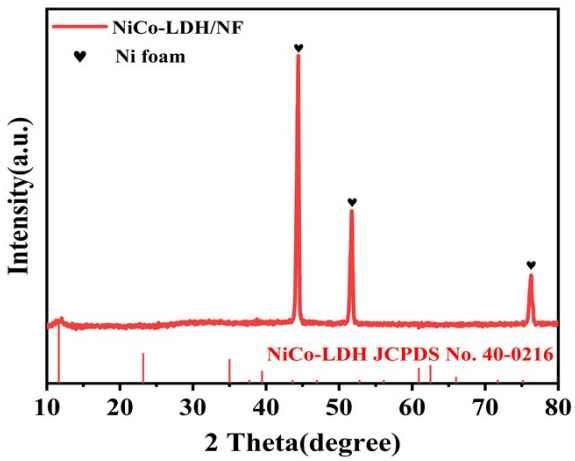

Figure S3. XRD pattern of NiCo-LDH/NF.

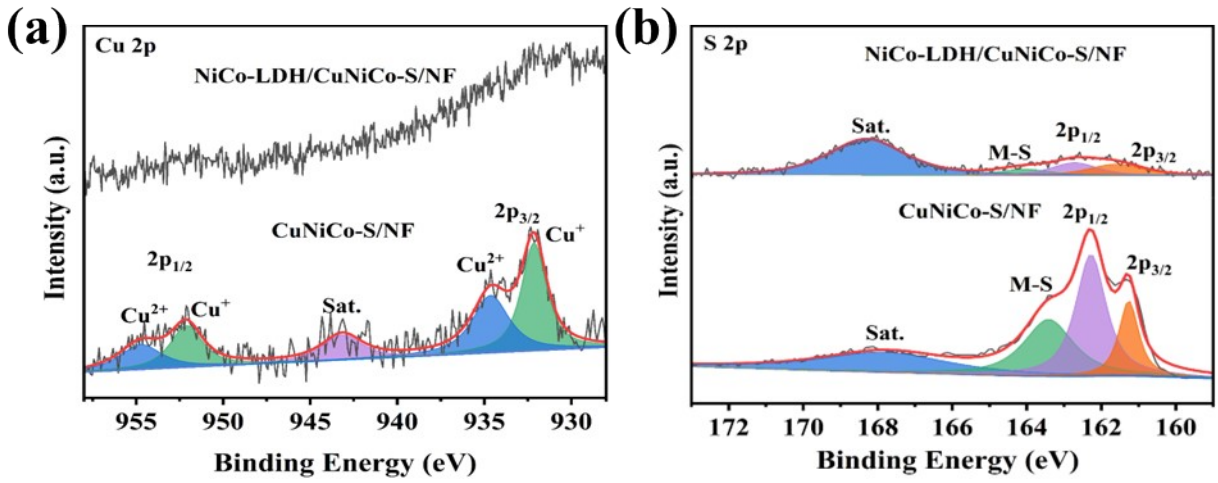

Figure S4. (a) Cu 2p and (b)S 2p XPS spectra of NiCo-LDH/CuNiCo-S/NF and CuNiCo-S/NF

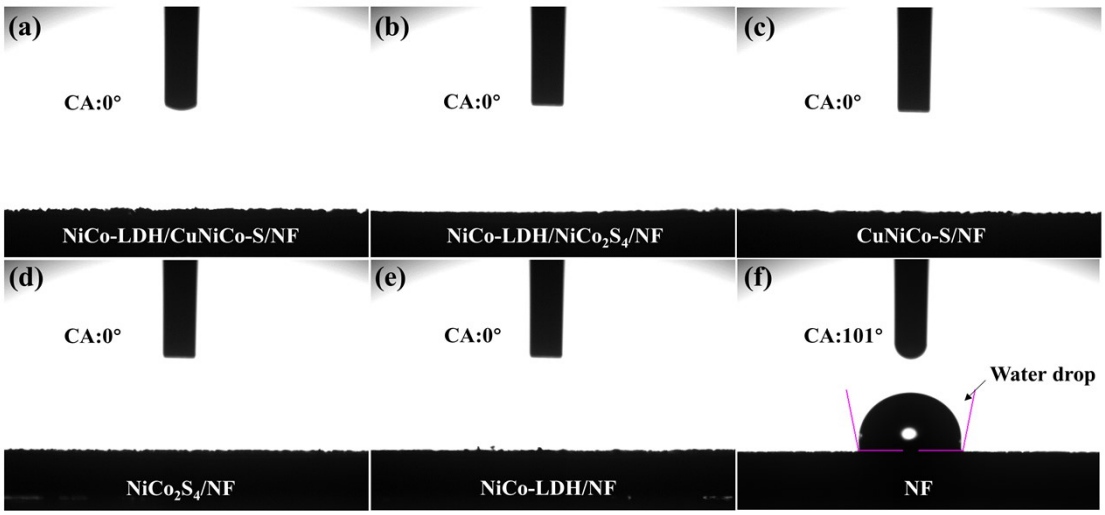

Figure S5. Static water droplet contact angles of NiCo-LDH/CuNiCo-S/NF, NiCo-LDH/$NiCo_2S_4$/NF, CuNiCo-S/NF, $NiCo_2S_4$/NF, NiCo-LDH/NF and NF.

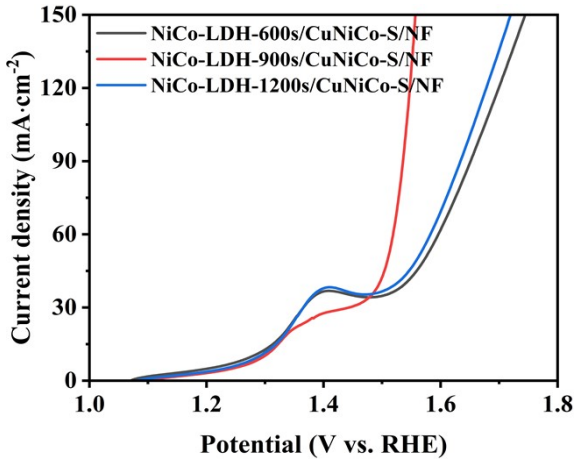

Figure S6. OER polarization curves of heterostructure with different deposition times

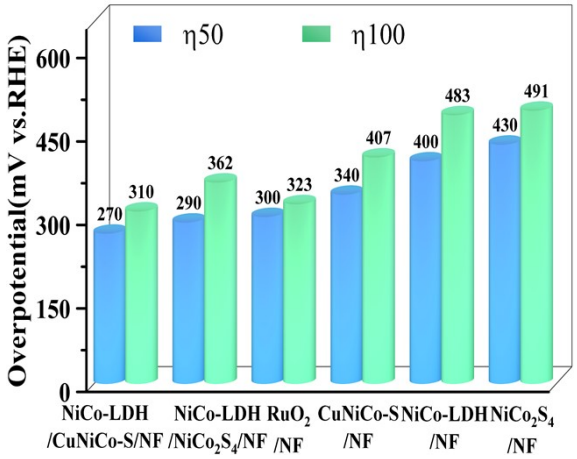

Figure S7. Overpotentials of the synthesized catalysts at 50 and 100 mA·cm^{-2}.

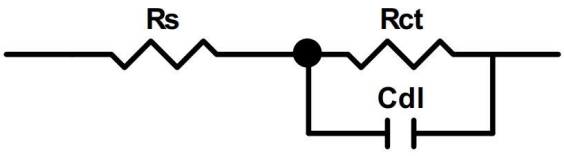

Figure S8. The equivalent circuit diagram used for the analysis of EIS curves.

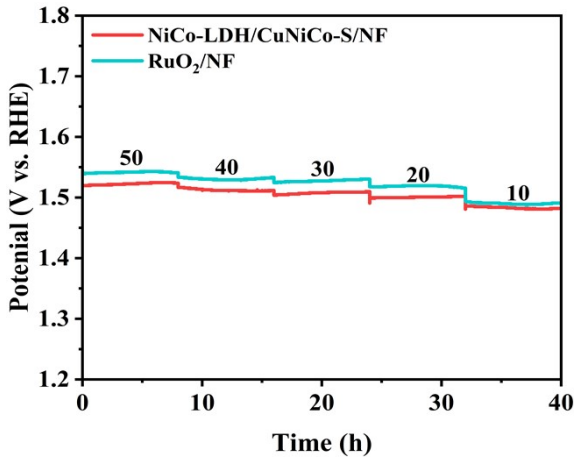

Figure S9. The comparison of stability between NiCo-LDH/CuNiCo-S/NF and RuO_2/NF.

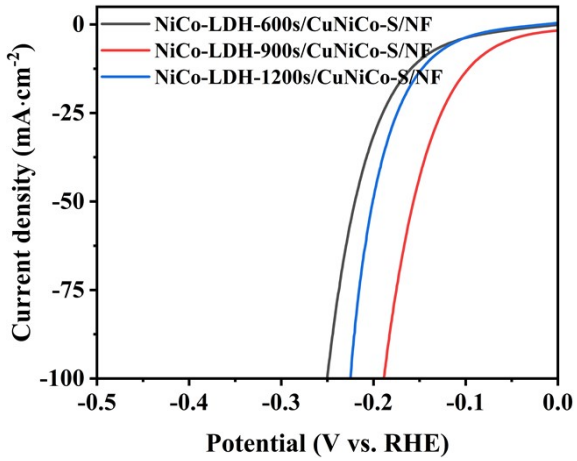

Figure S10. HER polarization curves of heterostructure with different deposition times

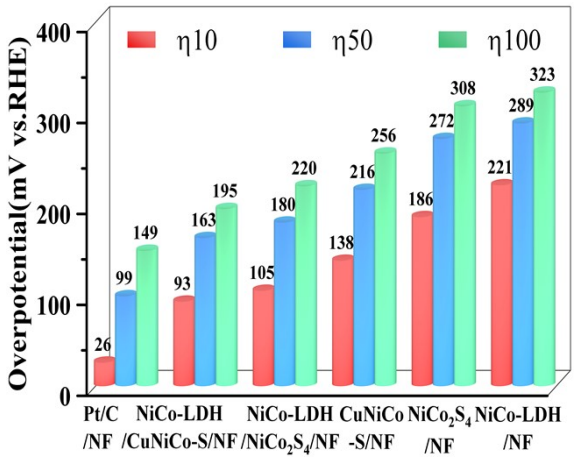

Figure S11. Overpotentials of the synthesized catalysts at 10, 50, and 100 mA·cm^{-2}.

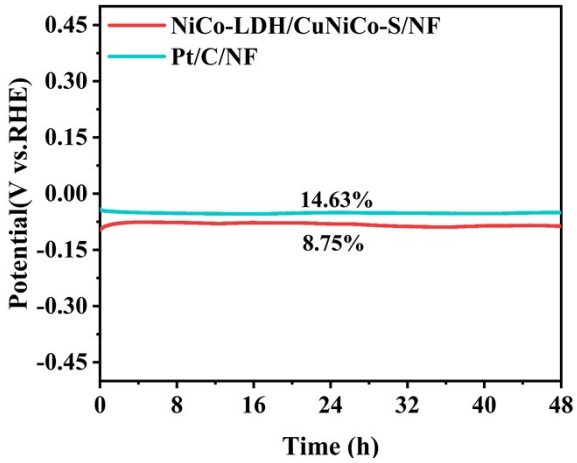

Figure S12. Chronopotentiometry curves of NiCo-LDH/CuNiCo-S/NF and Pt/C/NF at an invariable current density of 10 mA·cm^{-2} (the values shown in this graph indicate the increase rate of the potential).

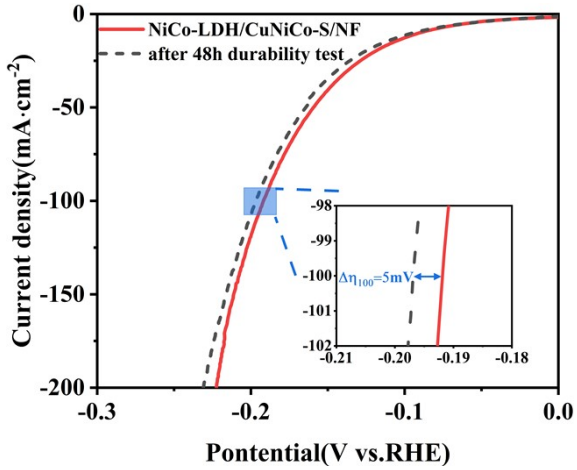

Figure S13. LSV curves of NiCo-LDH/CuNiCo-S/NF before and after the chronopotentiometry.

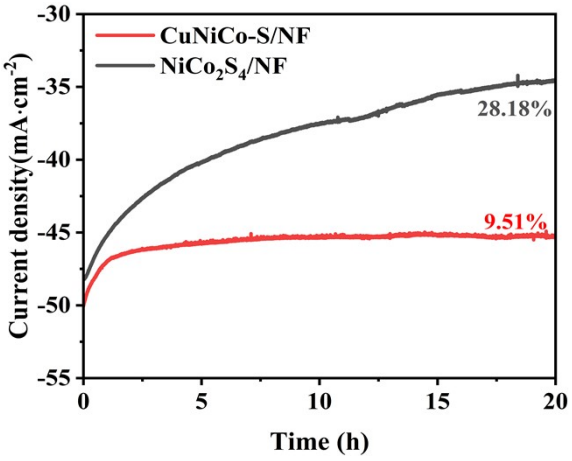

Figure S14. The comparison of stability between CuNiCo-S/NF and $NiCo_2S_4$/NF (the values shown in this graph indicate the decay rate of the current density).

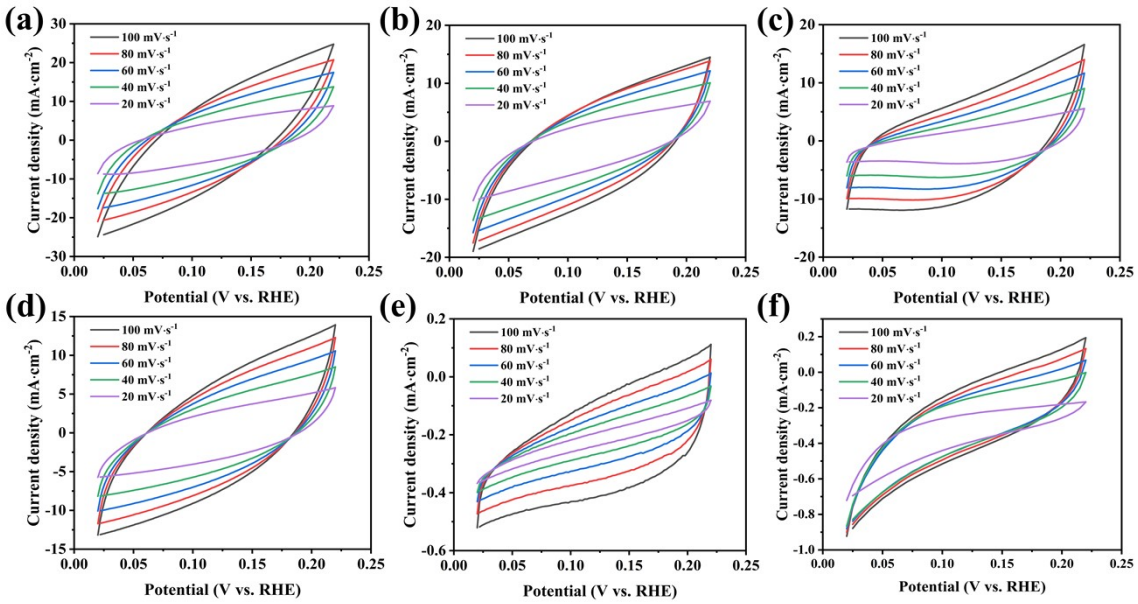

Figure S15. CV curves of (a)NiCo-LDH/CuNiCo-S/NF, (b) NiCo-LDH/ $NiCo_2S_4$/NF, (c) CuNiCo-S/NF, (d) $NiCo_2S_4$/NF, (e)NiCo-LDH/NF and (f) NF electrocatalysts at scan rates from 20 to 100 $mV \cdot s^{-1}$.

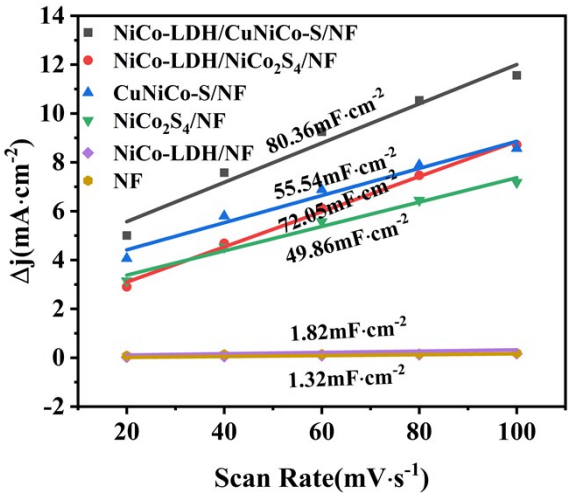

Figure S16. The relationship curves between current density and scan rate of NiCo-LDH/CuNiCo-S/NF, NiCo-LDH/$NiCo_2S_4$/NF, CuNiCo-S/NF, $NiCo_2S_4$/NF, NiCo-LDH/NF, and NF (the values shown in this graph indicate the C_{dl} of catalysts).

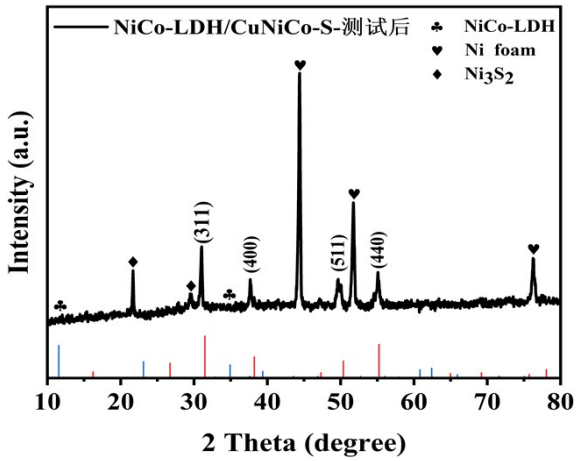

Figure S17. XRD pattern of NiCo-LDH/CuNiCo-S/NF after the test.

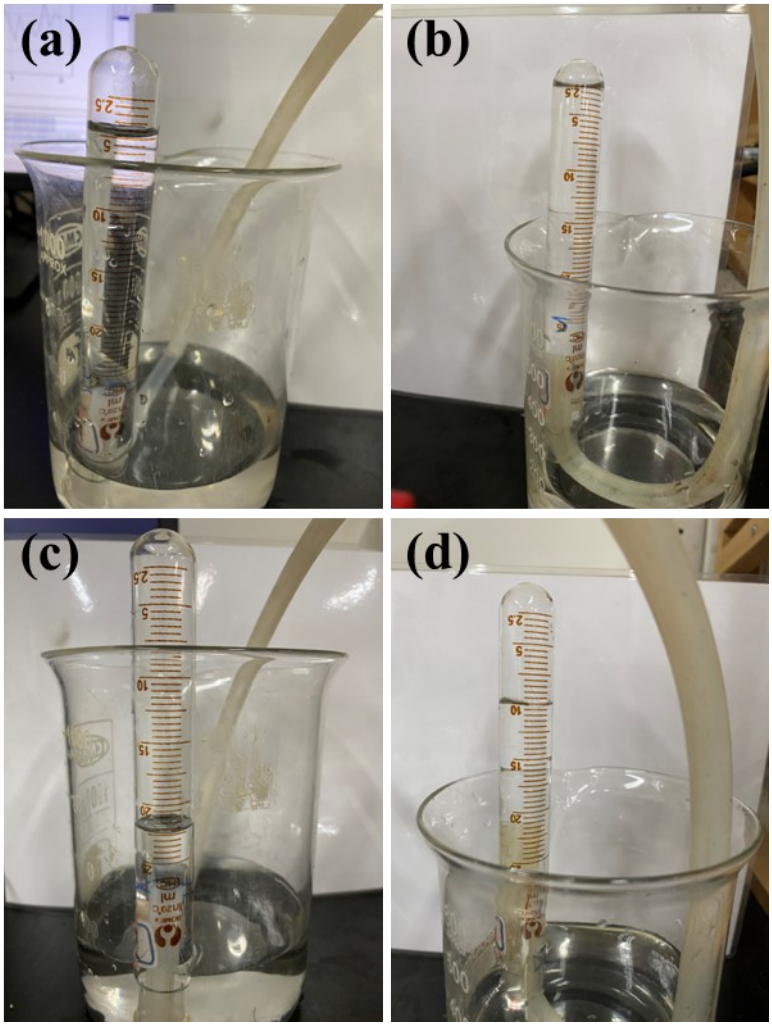

Figure S18. Schematic diagram of the gas production from two half-reactions during overall water splitting and at the end of the overall water splitting process.

Table S1. M^{3+}/M^{2+} intensity ratio of NiCo-LDH/CuNiCo-S/NF and NiCo-LDH/NF.

Catalysts M^{3+}/M^{2+}	Co^{3+}/Co^{2+}	Ni^{3+}/Ni^{2+}
NiCo-LDH/CuNiCo-S/NF	1.003/1.000	0.652/1.000
NiCo-LDH/NF	0.937/1.000	0.611/1.000

Table S2. Comparison of OER performances of NiCo-LDH/CuNiCo-S/NF and NiCo-LDH/$NiCo_2S_4$/NF electrocatalysts with other non-noble electrocatalysts in 1.0 M KOH or NaOH.

Catalysts	η_{50}	η_{100}	Tafel slope($mV \cdot dec^{-1}$)	Electrolyte	Reference
NiCo-LDH/CuNiCo-S/NF	**270**	**310**	**57.7**	**1.0 M KOH**	**This work**
NiCo-LDH/$NiCo_2S_4$/NF	**290**	**362**	**144.1**	**1.0 M KOH**	**This work**
Ni2V-MOFs@NF	287	314	38.1	1.0 M KOH	[2]
Ni-MOFs@NF	371	406	124.5	1.0 M KOH	[2]
NF@NiC	353		54	1.0 M KOH	[3]
Co-MOF/NF	311		77	1.0 M KOH	[4]
MIL-53(FeNi)/NF	233	244	31.3	1.0 M KOH	[5]
$NiO_X/NiCo_2O_4/Co_3O_4$	483		79	1.0 M NaOH	[6]
$NiCo_2S_4$/NF	371		91	1.0 M NaOH	[7]

Table S3. Comparison of HER performances of NiCo-LDH/CuNiCo-S/NF and NiCo-LDH/$NiCo_2S_4$/NF electrocatalysts with other non-noble electrocatalysts in 1.0 M KOH.

Catalysts	η_{10}	η_{50}	η_{100}	Tafel slope($mV \cdot dec^{-1}$)	Electrolyte	Reference
NiCo-LDH/CuNiCo-S/NF	**93**	**163**	**195**	**62.9**	**1.0 M KOH**	**This work**
NiCo-LDH/$NiCo_2S_4$/NF	**105**	**180**	**220**	**96.8**	**1.0 M KOH**	**This work**
Ni2V-MOFs@NF	89	197	235	98.3	1.0 M KOH	[2]
Ni-MOFs@NF	126	266	314	122.5	1.0 M KOH	[2]
NF@NiC	37			57	1.0 M KOH	[3]
Ni_3S_2@NiV-LDH/NF	126			90	1.0 M KOH	[8]
Co@N-CNT/NF	74	150		84	1.0 M KOH	[9]
NiCoSe MNSN/NF	85			52	1.0 M KOH	[10]
$P_{8.6}$-Co_3O_4 /NF	97			86	1.0 M KOH	[11]

Table S4. The C_{dl} values of different catalysts

Catalysts	**NiCo-LDH/CuNiCo-S/NF**	**NiCo-LDH/$NiCo_2S_4$/NF**	**CuNiCo-S/NF**	**$NiCo_2S_4$/NF**	**NiCo-LDH/NF**	**NF**
C_{dl}($mF \cdot cm^{-2}$)	**80.36**	**55.54**	**72.05**	**49.86**	**2.64**	**1.82**

Table S5. Comparison of two electrode water splitting cell voltage of NiCo-LDH/CuNiCo-S/NF electrocatalyst with other non-noble bifunctional electrocatalysts in 1.0 M KOH.

Catalysts	Cell voltage(V)	J/mA·cm^{-2}	Electrolyte	Reference
NiCo-LDH/CuNiCo-S/NF	**1.59**	**10**	**1.0 M KOH**	**This work**
$FeSe_2$/NF	1.73	10	1.0 M KOH	[12]
$MnCo_2O_4$@Ni_2P	1.63	10	1.0 M KOH	[13]
p-NiSe/NGr-CC	1.69	10	1.0 M KOH	[14]
CoP-N/Co foam	1.61	10	1.0 M KOH	[15]
Co_1Mn_1CH/NF	1.68	10	1.0 M KOH	[16]
Cu_3N-CuO	1.62	10	1.0 M KOH	[17]
CoP-HS	1.61	10	1.0 M KOH	[18]

References

1. X. Li, J. Zhou, C. Liu, L. Xu, C. Lu, J. Yang, H. Pang and W. Hou, Encapsulation of Janus-structured Ni/Ni_2P nanoparticles within hierarchical wrinkled N-doped carbon nanofibers: Interface engineering induces high-efficiency water oxidation, *Appl. Catal. B: Environ.*, 2021, **298**, 120578.

2. J. Lv, P. Liu, F. Yang, L. Xing, D. Wang, X. Chen, H. Gao, X. Huang, Y. Lu and G. Wang, 3D Hydrangea Macrophylla-like Nickel–Vanadium Metal–Organic Frameworks Formed by Self-Assembly of Ultrathin 2D Nanosheets for Overall Water Splitting, *ACS Appl. Mater. Interfaces*, 2020, **12**, 48495-48510.

3. H. Sun, Y. Lian, C. Yang, L. Xiong, P. Qi, Q. Mu, X. Zhao, J. Guo, Z. Deng and Y. Peng, A hierarchical nickel-carbon structure templated by metal-organic frameworks for efficient overall water splitting, *Energy Environ. Sci.*, 2018, **11**, 2363-2371.

4. X. P. Zhang, W. D. Sun, H. T. Du, R. M. Kong and F. L. Qu, A Co-MOF nanosheet array as a high-performance electrocatalyst for the oxygen evolution reaction in alkaline electrolytes, *Inorg. Chem. Front.*, 2018, **5**, 344-347.

5. F. Sun, G. Wang, Y. Ding, C. Wang, B. Yuan and Y. Lin, NiFe-Based Metal-Organic Framework Nanosheets Directly Supported on Nickel Foam Acting as Robust Electrodes for Electrochemical Oxygen Evolution Reaction, *Adv. Energy Mater.*, 2018, **8**, 1800584.

6. J. Chen, Y. Ling, Z. Lu, X. Huai and Z. Zhang, Sandwich-like NiO_x/$NiCo_2O_4$/Co_3O_4 nanoflakes enable efficient oxygen evolution electrocatalysis, *Electrochim. Acta*, 2019, **322**, 134753.

7. X. Yin, G. Sun, L. Wang, L. Bai, L. Su, Y. Wang, Q. Du and G. Shao, 3D hierarchical network $NiCo_2S_4$ nanoflakes grown on Ni foam as efficient bifunctional electrocatalysts for both hydrogen and oxygen evolution reaction in alkaline solution, *Int. J. Hydrogen Energy*, 2017, **42**, 25267-25276.

8. Q. Liu, J. Huang, Y. Zhao, L. Cao, K. Li, N. Zhang, D. Yang, L. Feng and L. Feng, Tuning the coupling interface of ultrathin Ni_3S_2@NiV-LDH heterogeneous nanosheet electrocatalysts for improved overall water splitting, *Nanoscale*, 2019, **11**, 8855-8863.

9. L. Yang, H. Li, Y. Yu, Y. Wu and L. Zhang, Assembled 3D MOF on 2D Nanosheets for Self-boosting Catalytic Synthesis of N-doped Carbon Nanotube Encapsulated Metallic Co Electrocatalysts for Overall Water Splitting, *Appl. Catal. B: Environ.*, 2020, **271**, 118939.

10. B. Liu, Y.-F. Zhao, H.-Q. Peng, Z.-Y. Zhang, C.-K. Sit, M.-F. Yuen, T.-R. Zhang, C.-S. Lee and W.-J. Zhang, Nickel-Cobalt Diselenide 3D Mesoporous Nanosheet Networks Supported on Ni Foam: An All-pH Highly Efficient Integrated Electrocatalyst for Hydrogen Evolution, *Adv. Mater.*, 2017, **29**, 1606521.

11. Z. Wang, H. Liu, R. Ge, X. Ren, J. Ren, D. Yang, L. Zhang and X. Sun, Phosphorus-Doped Co_3O_4 Nanowire Array: A Highly Efficient Bifunctional Electrocatalyst for Overall Water Splitting, *ACS Catal.*, 2018, **8**, 2236-2241.

12. C. Panda, P. W. Menezes, C. Walter, S. Yao, M. E. Miehlich, V. Gutkin, K. Meyer and M. Driess, From a molecular 2Fe-2Se precursor to a highly efficient iron diselenide electrocatalyst for overall water splitting, *Angew. Chem. Int. Ed.*, 2017, **129**, 10642-10646.

13. J. Ge, W. Zhang, J. Tu, T. Xia, S. Chen and G. Xie, Suppressed Jahn-Teller Distortion in $MnCo_2O_4$@Ni_2P Heterostructures to Promote the Overall Water Splitting, *Small*, 2020, **16**, 2001856.

14. A. Nadeema, P. S. Walko, R. N. Devi and S. Kurungot, Alkaline water electrolysis by NiZn-double hydroxide-derived porous nickel selenide-nitrogen-doped graphene composite, *ACS Appl. Energy Mater.*, 2018, **1**, 5500-5510.

15. Z. Liu, X. Yu, H. Xue and L. Feng, A nitrogen-doped CoP nanoarray over 3D porous Co foam as an efficient bifunctional electrocatalyst for overall water splitting, *J. Mater. Chem. A*, 2019, **7**, 13242-13248.

16. T. Tang, W.-J. Jiang, S. Niu, N. Liu, H. Luo, Y.-Y. Chen, S.-F. Jin, F. Gao, L.-J. Wan and J.-S. Hu, Electronic and morphological dual modulation of cobalt carbonate hydroxides by Mn doping toward highly efficient and stable bifunctional electrocatalysts for overall water splitting, *J. Am. Chem. Soc.*, 2017, **139**, 8320-8328.

17. C. Panda, P. W. Menezes, M. Zheng, S. Orthmann and M. Driess, In Situ Formation of Nanostructured Core–Shell Cu_3N–CuO to Promote Alkaline Water Electrolysis, *ACS Energy Lett.*, 2019, **4**, 747-754.

18. W. Zhang, N. Han, J. Luo, X. Han, S. Feng, W. Guo, S. Xie, Z. Zhou, P. Subramanian and K. Wan, Critical Role of Phosphorus in Hollow Structures Cobalt-Based Phosphides as Bifunctional Catalysts for Water Splitting, *Small*, 2021, DOI: 10.1002/smll.202103561, 2103561.